JOURNAL OF GEOPHYSICAL RESEARCH, VOL. 107, NO. D21, 4568, doi:10.1029/2001JD000646, 2002

Forest leaf area density profiles from the quantitative fusion of radar and hyperspectral data

Robert N. Treuhaft
Jet Propulsion Laboratory, California Institute of Technology, Pasadena, California, USA

Gregory P. Asner
Department of Global Ecology, Carnegie Institution, Stanford, California, USA

Beverly E. Law and Steven Van Tuyl
College of Forestry, Oregon State University, Corvalis, Oregon, USA

Received 20 March 2001; revised 8 October 2001; accepted 11 October 2001; published 7 November 2002.

[1] The leaf area density (LAD) of a forest is an important indicator of forest biomass and is therefore pertinent to monitoring carbon sequestration and change. Quantitative physical models were used to estimate forest LAD from radar and hyperspectral airborne remote sensing observations. A parameter-estimation technique based on physical models minimizes the need for in situ observations and thereby facilitates global remote sensing of forest structure. Using data from the NASA Airborne Synthetic Aperture Radar (AIRSAR) and the NASA Airborne Visible and Infrared Imaging Spectrometer (AVIRIS) over three forest plots in Central Oregon, parameters were estimated separately from the radar and hyperspectral data and then combined to form LAD. Gaussian relative LAD profiles were estimated from multialtitude interferometric and polarimetric AIRSAR data. Leaf area indices (LAI) were estimated from AVIRIS data and used to normalize the relative density profiles to produce LAD as a function of height. LAD was also determined from field measurements of geometric tree properties and LAI. LADs in the three forest plots were in the 0.02–0.18 $m^2\ m^{-3}$ range, with LAIs in the range 0.8–2.4 $m^2\ m^{-2}$. The agreement between the remotely sensed and field-measured LAD was typically 0.02 $m^2\ m^{-3}$ but occasionally as high as 0.06 $m^2\ m^{-3}$, which was within a 1–2 standard error range. More complex models for the remotely sensed relative density, along with more diverse radar observation strategies, will improve LAD accuracy in the future. LAD estimation will also improve when radar, hyperspectral, and other relevant remote sensing data sets are combined in a single parameter-estimation process, as opposed to the separate estimations performed in this first LAD demonstration. *INDEX TERMS:* 1030 Geochemistry: Geochemical cycles (0330); 0933 Exploration Geophysics: Remote sensing; 0315 Atmospheric Composition and Structure: Biosphere/atmosphere interactions; *KEYWORDS:* vegetation profiling, leaf area density, interferometric radar, hyperspectral imaging spectroscopy

Citation: Treuhaft, R. N., G. P. Asner, B. E. Law, and S. Van Tuyl, Forest leaf area density profiles from the quantitative fusion of radar and hyperspectral data, *J. Geophys. Res.*, *107*(D21), 4568, doi:10.1029/2001JD000646, 2002.

1. Introduction

[2] One of the principal objectives of forest remote sensing is determining the component of the global carbon budget affected by forest biomass sequestration and change [*Waring and Running*, 1998]. Vegetation structure, as revealed by density profiles, is a key indicator of aboveground biomass and biomass change due to natural or anthropogenic disturbance [*Whitehead*, 1978]. This paper describes the first remotely sensed determination of the forest-structure variable, leaf area density (LAD). LAD is the total one-sided leaf surface area per unit volume in the canopy [*Myneni et al.*, 1989]. It is averaged over a specified lateral area and is expressed as a function of height above the ground. In this paper, LAD will be determined by the quantitative fusion of radar data from the NASA Airborne Synthetic Aperture Radar (AIRSAR) [*Zebker et al.*, 1992] and hyperspectral data from the Airborne Visible and Infrared Imaging Spectrometer (AVIRIS) [*Green et al.*, 1998].

1.1. Motive For Measuring Leaf Area Density

[3] Because LAD is the distribution of leaf area as a function of height, z, it depends on species, developmental stage, and disturbance, all of which influence levels of standing biomass. Figure 1 qualitatively illustrates how two height distributions would result in two very different LADs and would contribute in very different ways to a

0148-0227/02/2001JD000646$09.00

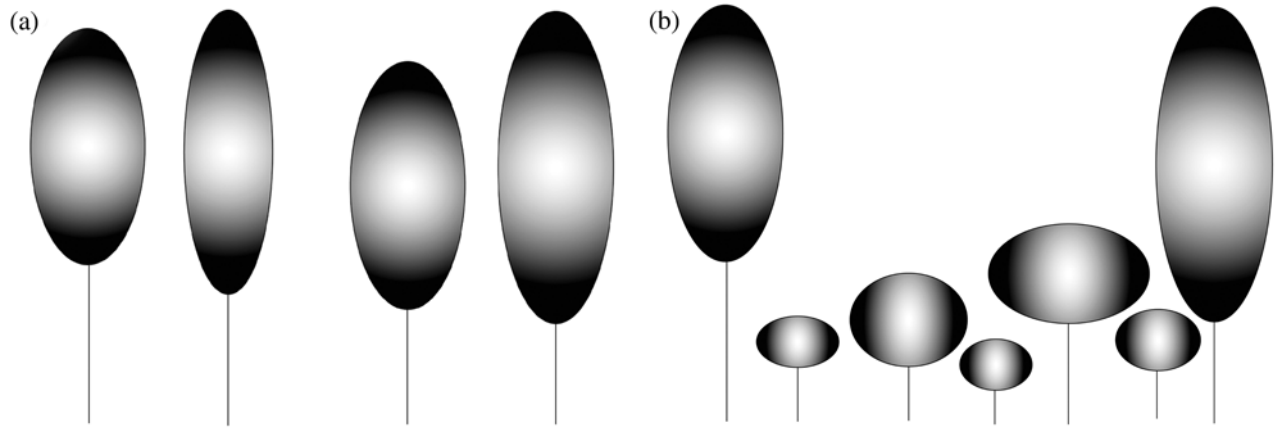

Figure 1. (a) Schematic picture of a stand with fairly uniform tree height. (b) More diverse height distribution due to disturbance and regrowth.

carbon budget. Figure 1a schematically shows a stand with fairly uniform tree heights. Figure 1b shows a stand with more diverse heights, characterized by sparse, tall, old growth and dense, young regrowth. The LAD from Figure 1a would probably have a maximum density near the center of the tree canopy, while the LAD from Figure 1b might have a maximum at lower heights, with a tail extending up to the higher values of z corresponding to the tallest trees in the stand. Figure 1a could represent a mature forest characterized by large biomass and substantial carbon storage. Figure 1b could represent a forest that has undergone recent biomass loss through disturbance, with subsequent biomass accumulation as regrowth and overall LAD increase.

[4] The output of this work, LAD, is thus an important input to ecosystem process models that simulate the role of terrestrial vegetation in the global carbon cycle [*Sellers*, 1997]. Biomass and structural characteristics are also employed in many models, which investigate the influence of climate, disturbance, or developmental stage on the processes controlling net carbon uptake by ecosystems [e.g. *Williams et al.*, 2001; *Law et al.*, 2000; *Law et al.*, 1999; *Cohen et al.*, 1996; *Landsberg and Waring*, 1997]. These models, which are applied at the stand, regional or global level, require the spatial estimates of canopy structure developed in this paper.

1.2. Motive for Remote Sensing by Quantitative Data Fusion

[5] Forests are sufficiently complex targets that a single remote sensing technique is typically incapable of accurately characterizing the structural attributes needed to determine biomass and carbon dynamics. For example, a single-baseline radar interferometric phase observation over a forest cannot be uniquely related to either the surface topography or the height of the vegetation but will represent some combination of the two [*Hagberg et al.*, 1995; *Askne et al.*, 1997; *Wegmuller and Werner*, 1997; *Rosen et al.*, 2000]. With interferometric amplitudes and phases from two or more baselines [*Treuhaft et al.*, 1996], or with a set of interferometric observations at different polarizations [*Cloude and Papathanassiou*, 1998], vegetation height and surface topography begin to be separable.

[6] Analogous to the microwave domain, the broadband normalized difference vegetation index (NDVI) [*Tucker and Sellers*, 1986] in optical remote sensing, with its wide $\sim$0.3 μm bandwidths, is not capable of accurately estimating leaf area indices (LAI, the integral of LAD(z) up to the canopy height) above values of 4–5 [*Diner et al.*, 1999]. The addition of many more narrow spectral channels allows determination of much higher LAI values [*Gao and Goetz*, 1990, 1995; *Ustin et al.*, 1998]. Additionally, specialized hyperspectral observations in the shortwave-infrared (2.0–2.4 μm) allow for the determination of subpixel canopy cover fraction independent of canopy LAI [*Asner and Lobell*, 2000; *Lobell et al.*, 2001]. Canopy cover fraction is necessary for modeling shadowing effects during the process of LAI estimation.

[7] In general, a set of data types, which exhibit diverse sensitivities to forest parameters of interest, yields more accurate parameter estimates than those derived from any single data type [*Kynazikhin et al.*, 1998]. The diversity of sensitivities of radar and hyperspectral data to LAD renders their combination suitable to LAD determination, although either technique alone would be insufficient.

[8] One advantage of using a physical-model approach to remote sensing is that minimal in situ measurements are needed. The remote sensing is truly ''remote'' and has much greater potential for global monitoring than nonphysical approaches that require in situ training. Because the model-driven estimation process also yields parameter-estimate errors as a function of the diversity of observations and their errors, systematic paths to accuracy improvement can be explored; they can be assessed with a priori covariance analyses and can then be tested with data. The disadvantage of relying on physical models is that model inaccuracy or oversimplification will corrupt results such as LAD. The best way to test the accuracy and completeness of models is to apply them to real remote sensing data and compare the parameters estimated to field-measured results, as in this paper.

[9] Section 2 of this paper describes the AIRSAR (radar), AVIRIS (hyperspectral), and field data acquisitions. The parameter-estimation approach to quantitative fusion is detailed in section 3. The physical models required for parameter estimation and their specified dependence of

the radar and hyperspectral data on model parameters are described in sections 4 and 5, respectively. Section 6 describes the estimation of LAD from field data from three ponderosa pine (*Pinus ponderosa* Var. Laws) stands in central Oregon. In section 7, the remotely sensed LADs derived from the methods in sections 3, 4, and 5 are compared with the field measurements of section 6. Section 8 contains conclusions and future plans.

2. Radar, Hyperspectral, and Field Data Acquisitions

[10] AIRSAR was flown on 25 April 1998 in interferometric mode, with vertical polarization, over Central Oregon at three different altitudes, 8, 4, and 2 km. As will be shown in section 4, multibaseline radar interferometry, which can be acquired by flying a single baseline at multiple altitudes, enables estimates of the LAD profile as a function of height above the ground. Radar interferometric data were collected at wavelengths of 5.7 cm (C band) with a physical baseline of 2.46 m and at 24.2 cm (L band) with a physical baseline of 1.97 m. Only the C band data had a sufficiently large baseline/(wavelength $\times$ altitude) ratio to be useful in the parameter-estimation process in section 3; the L band data were analyzed but not reported here because they added little to the LAD determination. Polarimetric data were also acquired at 8 km, at C, L, and P band (68.3 cm), but only C band data were used. The AIRSAR DC8 flight path was shifted for each altitude to maintain the same target at a 35° look angle. The average longitude and latitude of the overflight was $-121.70°$ and 44.44°, and the flight spanned an area of $\sim 20 \times 20$ km. This area contained twenty stands on which assorted field measurements were made. This study focuses on three of those twenty, as noted below.

[11] AVIRIS collects upwelling radiance data in 224 optical channels with a nominal resolution of 10 nm covering a spectral range of 380–2500 nm [*Green et al.*, 1998]. The AVIRIS was flown over the study region on 10 June 1999 on the NASA ER-2 aircraft at 20 km altitude, creating $\sim 17 \times 17$ m pixels in the resulting image data. Radiance data were converted to apparent surface reflectance using the ATREM atmospheric code [*Gao et al.*, 1993], which employs the 6S scattering code for atmospheric gases [*Vermote et al.*, 1997]. Further corrections for surface reflectance were made using a large (dark) lake and (bright) cumulous clouds [*Lobell et al.*, 2001].

[12] Field observations were performed on 20 stands including the two Metolius flux sites in Central Oregon in summer 1999. The flux sites are part of the eddy flux networks, AmeriFlux and Fluxnet, and they are NASA EOS Land Validation Core sites (http://modis-land.gsfc.nasa.gov/val/). Forest structure was measured on each of the twenty 100×100 m plots. Total tree height, height at the widest point of the crown, crown radius, and height at the base of the crown were measured using a laser clinometer (Impulse 200, Laser Technology, Englewood, Colorado) and stem diameter using a diameter tape. Measurements were made on all trees greater than 5 cm DBH (diameter at breast height, 1.4 m), and the remaining trees were tallied. GPS coordinates were obtained for each of the stands, as well as for prominent features such as major road intersections, to facilitate radar geolocation.

[13] LAI was also measured on each of the forest stands on a 10 m grid using an optical leaf area meter (LAI-2000, LICOR, Lincoln, Nebraska), resulting in 121 measurement points per plot. Measurements were made under diffuse sky conditions, primarily in the evening. A mean value for LAI was calculated for each plot and then corrected for canopy clumping using the methods described by *Chen et al.* [1997] and *Law et al.* [2001a]. Three stands were identified for field LAD estimation, as described in section 6.

3. Parameter-Estimation Approach to Quantitative Fusion

[14] This section formulates the parameter estimation approach to the radar and hyperspectral data for estimating LAD. It will describe the inputs to and outputs from the physical model in Figure 2, which schematically shows the process of determining LAD(z) from radar and hyperspectral observations. The physics relating the outputs to the inputs will be described in sections 4 and 5. The "other params" in Figure 2 represent other parameters required by the physical model that will also be estimated. They include, for example, surface topography [*Treuhaft et al.*, 1996] or subpixel canopy cover fraction [*Lobell et al.*, 2001]. These other parameters will be specifically used in future analyses to understand stand succession, but this paper will focus on LAD.

[15] Figure 2 represents what is referred to in this paper as "quantitative fusion." The fusion of radar and hyperspectral data is quantitative in that physical mechanisms based on electromagnetic propagation relate LAD to each data type via the physical model. The physical-model approach in this paper is based on discrete scatterers (microwave) [*Treuhaft et al.*, 1996] and radiative transport (hyperspectral-optical) [*Asner*, 1998; *Asner*, 2000]. Figure 2 is idealized in that it shows microwave and hyperspectral data as entering the analysis together, being processed by a single model as in equation (2), and the model-data difference being minimized in a single parameter estimation approach. In order to optimize quantitative fusion, the data should be processed together as shown in Figure 2. However, in this first demonstration of quantitative fusion, an operationally easier approach is taken in which the two data types are processed separately, as explained below.

[16] The parameter-estimation process adopted for the AIRSAR and AVIRIS data involves expressing LAD(z) in terms of a small set of parameters and estimating those parameters from the radar and hyperspectral data. To that end, LAD(z) is represented in terms of a normalized (vertical integral = 1) relative-density function Rel($z;\vec{P}$) and the LAD integrated in the vertical direction:

$$\mathrm{LAD}(z) = \left[\int_0^\infty dz'\ \mathrm{LAD}(z')\right] \mathrm{Rel}(z;\vec{P}) \equiv \mathrm{LAI}\ \mathrm{REL}(z;\vec{P}) \quad (1)$$

The relative-density function is similar to the profile that can be obtained from lidar [*Lefsky et al.*, 1999]. In equation (1), $\vec{P}$ is a set of parameters on which the relative density Rel($z;\vec{P}$) depends, for example, a slope and an intercept for a linear density as a function of height. In this paper, $\vec{P}$ will be the center and standard deviation of a Gaussian density function. In equation (2), the model M is represented by its operation on the input LAD parameters in (1), Rel($z;\vec{P}$) and

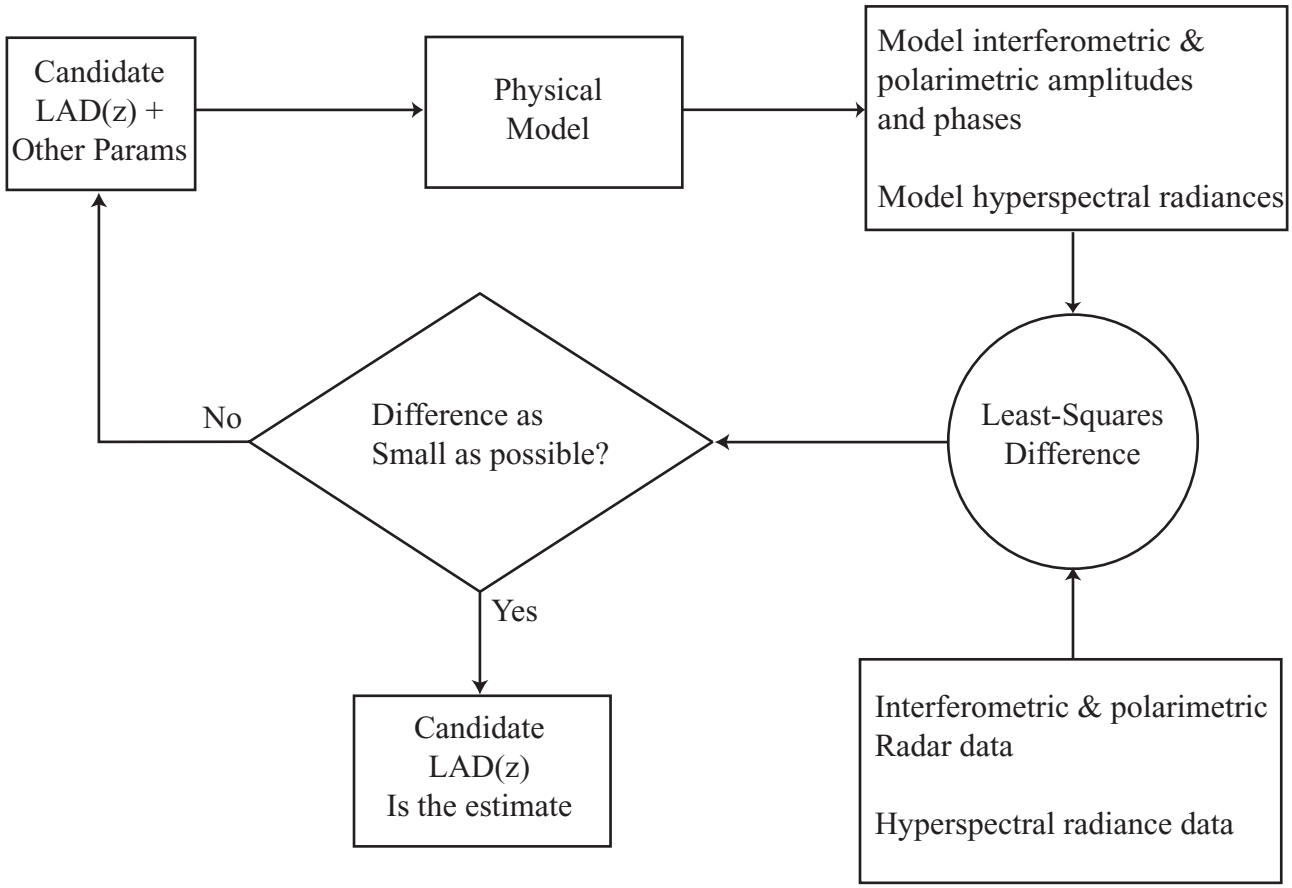

Figure 2. Schematic representation of LAD parameter estimation using interferometric and polarimetric radar and hyperspectral optical data.

LAI, and other parameters required to produce the radar and hyperspectral observations on the left side:

$$\begin{pmatrix} \text{Interrefometric Phase}_1 \\ \text{Interferometric Coherence}_1 \\ \vdots \\ \text{Interferometric Phase}_Q \\ \text{Interferometric Coherence}_Q \\ \text{Polarimetric Power Ratio} \\ - - - - - - - - - - - \\ \text{Hyperspectral Reflectance}_1 \\ \vdots \\ \text{Hyperspectral Reflectance}_R \end{pmatrix} = \mathbf{M}\begin{pmatrix} \text{LAD(z)} \\ \text{Other Parameters} \end{pmatrix}$$

$$= \mathbf{M}\begin{pmatrix} \text{Rel}(\mathbf{z}, \vec{\text{P}}) \\ \text{LAI} \\ \text{Other Parameters} \end{pmatrix} \quad (2)$$

The interferometric coherence is the amplitude of the cross correlation (equation (4)), normalized by the square root of the power at each end of the baseline and varies between 0 and 1. The indices on the coherences and phases refer to Q different baselines or altitudes in this paper but could also indicate different observing wavelengths, different polarimetric combinations at the end of a single baseline, or any combination of the above. The polarimetric power ratio is the ratio of received power in horizontal polarization to that in vertical polarization. The hyperspectral entries represent R high-resolution channels in the 0.4–2.4 μm range. The model **M** in equation (2) is the microwave and optical physical models, represented as a single physical model in Figure 2.

[17] The Rel(z;$\vec{\text{P}}$) and LAI parameters on the right side of equation (2) were chosen to express LAD(z) because they are easily related to the radar and hyperspectral observations, respectively, with simple models. While changes in either of these top two entries affect both radar and hyperspectral data, in this first attempt at estimating LAD, Rel(z;$\vec{\text{P}}$) was assumed to affect only radar data and LAI was considered to affect only hyperspectral data. The version of equation (2) actually used to derive LAD from AIRSAR and AVIRIS data associates Rel(z;$\vec{\text{P}}$) and LAI with radar and hyperspectral data, respectively, as follows:

$$\begin{pmatrix} \text{Interferometric Phase}_1 \\ \text{Interferometric Coherence}_1 \\ \vdots \\ \text{Interferometric Phase}_Q \\ \text{Interferometric Coherence}_Q \\ \text{Polarimetric Power Ratio} \end{pmatrix} = M_{radar}\begin{pmatrix} \text{Rel}(\text{z}, \vec{\text{P}}) \\ \text{Other Radar Parameters} \end{pmatrix} \quad (3)$$

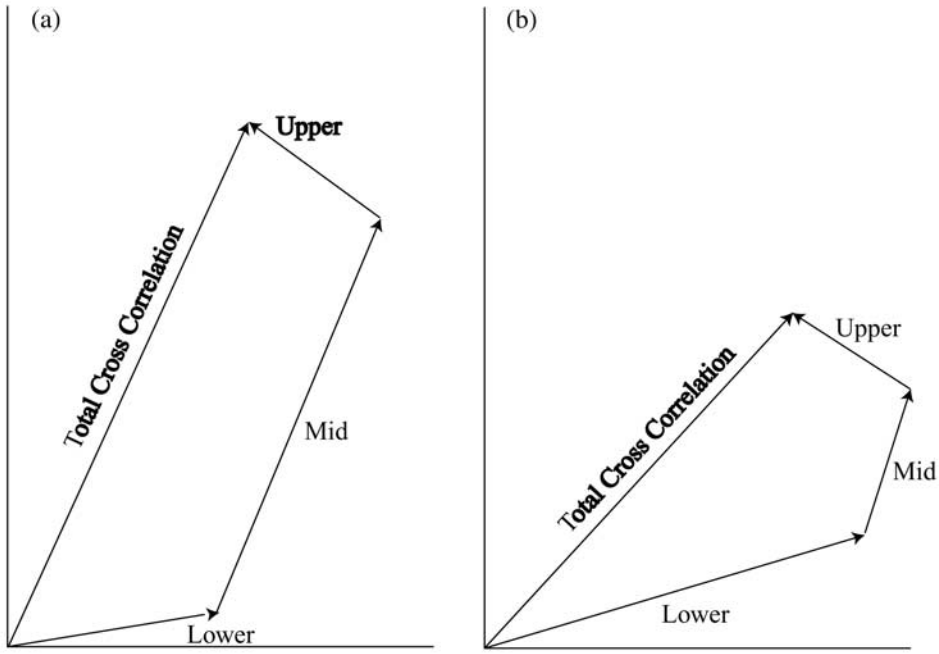

Figure 3. (a) Schematic vegetation contributions to the interferometric cross correlation from a hypothetical three-level vegetation density distribution peaked in the middle, with a (b) maximum density at the lowest level. The length of each line corresponds to the cross-correlation amplitude, and the angle that each line makes with the x axis is the cross-correlation phase.

$$\begin{pmatrix} \text{Hyperspectral Reflectance}_1 \\ \vdots \\ \text{Hyperspectral Reflectance}_R \end{pmatrix} = M_{hyper} \begin{pmatrix} \text{LAI} \\ \text{Other Hyperspectral Parameters} \end{pmatrix}$$

The separate estimation of parameters from radar and hyperspectral data in equation (3) loses some of the benefits of quantitative fusion because the dependence of, for example, hyperspectral observations on $\mathrm{Rel}(z;\vec{\mathrm{P}})$, is ignored in the radar-only determination of $\mathrm{Rel}(z;\vec{\mathrm{P}})$. Modeling this dependence and performing a combined estimation as in equation (2) might improve the determination of the LAI parameter and thus of LAD in the future.

4. Leaf Area Density Parameters From the Radar Physical Model

[18] This section will describe the radar model in equation (3) that expresses the radar interferometric and polarimetric observations as a function of the radar LAD parameter ($\mathrm{Rel}(z;\vec{\mathrm{P}})$) and other radar parameters. The complete set of parameters is determined by the physical model, which involves both a distorted-Born, randomly oriented vegetation volume and a ground component [*Treuhaft and Siqueira*, 2000]. The coherence and phase of the complex interferometric cross correlation is the fundamental interferometric observation. In this work, the polarimetric power ratio (power at horizontal polarization/power at vertical polarization) is the only polarimetric quantity considered, but the approach to including all possible polarimetric and polarimetric interferometric quantities in terms of physical model parameters is given by *Treuhaft and Siqueira* [2000].

[19] Representing the coherence (the amplitude of the cross correlation normalized by the total power) by the length of lines, and representing the phase by the angle the line from each vegetation component makes with the x axis, Figure 3 schematically shows how vegetation components at each level in a hypothetical three-layer canopy add to form the normalized cross correlation. In Figure 3a, a profile is represented in which the vegetation contributes the strongest signal in the middle of the canopy, as in Figure 1a. Figure 3b represents a distribution like that of Figure 1b in which the lower part of the canopy gives the strongest radar returns and the mid and upper parts are weaker. Note that both the coherence and the phase of the total cross correlation change if the structure, which is related to $\mathrm{Rel}(z;\vec{\mathrm{P}})$, changes. Because the phase angle of each line is also proportional to the baseline length, a family of total cross correlations results from a set of baselines used to observe the structure of a given forest stand.

[20] There is both a vegetation volume and ground component to the quantitative description of the cross correlation in equation (4). The vegetation volume component, which is the first term in equation (4), derives from *Treuhaft et al.* [1996, equation C7]. The ground component, which is the second term in equa-

tion (4), derives from *Treuhaft and Siqueira* [2000, equation 24]:

$$\text{Cross Correlation} \propto e^{i\phi(z_0)} \int_0^\infty dz\, e^{i\alpha_z(\frac{B}{\lambda H})z} N(z)\langle f_b^2(z)\rangle \times \exp\left[\frac{2}{\cos\theta_0}\int_0^z dz'\sigma_x(z')\right] + 4\Delta_{\hat{V}}(\psi,\varepsilon)e^{i\phi(z_0)} \quad (4)$$

The integral over z continuously sums the cross correlation weighted by the vegetation scattering strength at each altitude, as represented discretely in Figure 3. The strength is the product of the number of scatterers per unit volume, $N(z)$, and the average squared backscattering amplitude, or strength, of a single scatterer, $\langle f_b^2\ (z)\rangle$. This strength is weighted at each altitude by attenuation in the integral over z', which contains the profile of the microwave extinction coefficient, $\sigma_x(z)$. In equation (4), θ_0 is the angle between the vertical pointing down, along the $-z$ direction from the radar, and the patch of forest being observed, and $\alpha_z(B/(\lambda H))$ is the derivative of interferometric phase with respect to altitude above the surface. It is proportional to B, the baseline length, over λH, the radar wavelength times the aircraft altitude. The dependence of the cross correlation on B/H prompts varying H, the AIRSAR altitude, to achieve an effective variation in baseline length. The term $\phi(z_0)$ is the interferometric phase at the ground altitude, z_0, and is close to the phase of the lowest vegetation component in Figure 3. Since the volume is assumed randomly oriented, the scattering-amplitude terms are not polarimetrically sensitive [*Treuhaft and Cloude*, 1999]. Although leaves and other canopy material are characterized by apparent systematic orientations, there is no evidence that vegetation volume orientation has any detectable effect on microwave scattering in forests as observed with interferometry.

[21] The second term in equation (4) is the ground contribution, contributing a phase of $\phi(z_0)$ with a strength $4\Delta_{\hat{V}}(\psi,\varepsilon)$, where $\hat{V}$ refers to vertical polarization, ψ is a term having to do with ground roughness, and ε is the ground dielectric constant [*Treuhaft and Siqueira*, 2000]. The horizontally oriented ground carries the only polarimetric signature. The parametric dependence of the final radar observation in equation (3), the polarimetric power ratio, is obtained from equation (4) by letting the baseline go to zero, evaluating at both horizontal and vertical polarizations, and taking the ratio.

[22] The goal of the model in equation (4) is to relate the cross correlation to the vegetation structure parameter to be estimated, $\text{Rel}(z;\vec{P})$, as well as whatever "other" parameters are required, as indicated in equation (3). This is accomplished by the following model assumptions relating $\text{Rel}(z;\vec{P})$ to the geometric and electromagnetic terms in equation (4):

$$\begin{aligned} N(z)\langle f_b^2(z)\rangle &\propto \text{Rel}(z;\vec{P}) \\ \sigma_x(z) &\equiv \sigma_{x0}\,\text{Rel}(z;\vec{P}) \end{aligned} \quad (5)$$

In order to see why the assumption in the first line of (5) is plausible, consider that

$$LAD(z) \propto \text{Rel}(z;\vec{P}) \approx \frac{Number\ of\ Leaves}{Volume}(z) \times Average\ Area\ per\ Leaf\ (z) \quad (6)$$

Given (6), the assumption in the first line of (5) effectively says that the number of microwave scatterers per unit volume, N(z), is proportional to the number of leaves (needles) per unit volume, which is a reasonable assumption. Even if the fundamental scatterers, for example at lower radar frequencies, are branches, the number of those scatterers per unit volume is probably still proportional to the number of leaves per unit volume as a function of altitude, for many forests. It is also plausible that the average area per leaf is related to the backscattering strength, $\langle f_b^2(z)\rangle$. Alternatively, it is a plausible modeling assumption that the average backscattering strength of a single scatterer has a much weaker z-dependence than the scatterer number density, in which case the first line of (5) still holds. The extinction coefficient in the second line of (5) is also proportional to N(z) and to scattering characteristics [*Treuhaft et al.*, 1996]. The second line of (5) is plausible by similar arguments.

[23] Using (5) in (4), and assuming that the relative leaf area density is Gaussian yields a model, M_{radar}, relating the radar observations to $\text{Rel}(z;z_G,\sigma_G)$ and other parameters:

$$\text{Cross Correlation} \propto e^{i\phi(z_0)} \int_0^\infty dz\, e^{i\alpha_z(\frac{B}{\lambda H})z}\,\text{Rel}(z;z_G,\sigma_G) \times \exp\left[\frac{2}{\cos\theta_0}\int_0^z dz'\sigma_{x0}\,\text{Rel}(z';z_G,\sigma_G)\right] + 4\Delta_{\hat{V}}(\psi,\varepsilon)e^{i\phi(z_0)} \quad (7)$$

where z_G is the center of the Gaussian density distribution and σ_G is the standard deviation. The Gaussian profile parameterization is motivated by the field observations of LAD, but estimation of more complex profiles, for example a double-Gaussian, should be tried with remote sensing data sets that are more extensive than those analyzed here.

[24] The dependence of the total cross correlation on $\text{Rel}(z;z_G,\sigma_G)$ and other parameters results from (7), prompting the expression for microwave data below:

$$\begin{pmatrix} \left\{\begin{array}{l} \text{Interferometric Phase}_{\text{i km}} \\ \text{Interferometric Coherence}_{\text{i km}} \\ \text{Interferometric Phase}_{\text{i km ping}} \\ \text{Interferometric Coherence}_{\text{i km ping}} \end{array}\right\} \\ \text{Horizontal/Vertical Power Ratio} \end{pmatrix} = \text{M}_{radar} \begin{pmatrix} \sigma_{x0} \\ z_G \\ \sigma_G \\ \psi \\ \varepsilon \\ z_0 \end{pmatrix} \quad (8)$$

where the set of observations in the curly brackets are specified by the subscripts, i, which indicate the radar altitudes 8, 4, and 2 km. The subscript "ping" indicates ping-pong interferometric mode, in which signals are alternately transmitted from each end of the baseline. This mode effectively doubles the baseline length without changing the altitude [*Treuhaft and Siqueira*, 2000]. The HHHH/VVVV entry is the ratio in the power transmitted and received at horizontal polarization to that at vertical polarization. This is the only polarimetric observation used, as introducing more polarimetric observations requires the introduction of more parameters describing the scatterers and does not improve the

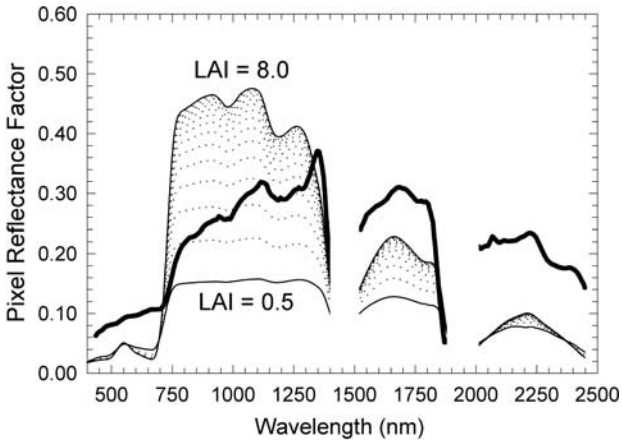

Figure 4. Canopy reflectance as a function of wavelength for a range of LAI values with no non-photosynthetic tissue exposure. A typical AVIRIS spectrum from the Oregon imagery is also shown in the bold line.

structure determination [*Treuhaft and Siqueira*, 2000]. This polarimetric ratio helped to control the parameter estimates, but the multialtitude interferometric observations were much more influential in determining the profile parameters. Two phase offset parameters not shown in (8) were also estimated in order to remove the effects of systematic errors found in AIRSAR interferometric phases.

5. Leaf Area Density Parameters From the Hyperspectral Physical Model

[25] This section will describe the hyperspectral model in (3) that relates LAD parameters (LAI and other vegetation parameters) to the hyperspectral reflectances. These parameters are derived from the numerical inversion of a physical model that relates the scattering and absorption properties of vegetation elements in 3-dimensional space to the observed pixel spectroscopic reflectance from AVIRIS [*Asner*, 1998, 2000; *Asner et al.*, 1998b]. The total one-sided LAI is the vertically integrated LAD, as indicated in (1).

[26] Figure 4 shows the qualitative dependence of the hyperspectral reflectance spectrum on LAI. The AVIRIS spectrum acquired for plot 1 of the Oregon forest sites is also shown with the heavy line, indicating the approximate LAI by simple inspection of the visible/near-IR spectral region between 0.68 and 1.2 μm. The "red-edge" (0.69–0.71 μm) is particularly sensitive to increasing LAI [*Hall et al.*, 1990], as are the local canopy water absorption features near 0.9 and 1.2 μm [*Gao and Goetz*, 1995; *Ustin et al.*, 1998]. However, pronounced non-photosynthetic tissue absorption features in the short-wave-infrared (2.0–2.4 μm) region of the AVIRIS spectrum indicate the presence of exposed ground litter, which is due to partial canopy cover within the pixel [*Asner*, 1998]. Exposed ground cover is also indicated by the lack of a strong "green peak" near 0.55 μm in the AVIRIS spectrum.

[27] The spectral dependence of the reflectance signatures in Figure 4 is a function of the illumination and viewing geometry, canopy structure, and tissue optical properties. These parameters come together in the radiative transfer equation governing the pixel-scale reflectance, at wavelength λ, as observed by the sensor:

$$\rho_{pixel}(\lambda,\Omega',\Omega) = [VC \times \rho_{canopy}(\lambda,\Omega',\Omega)] + [(1-VC) \times \rho_{ground} \cdot (\lambda,\Omega',\Omega)] \quad \text{or}$$

$$\rho_{pixel}(\lambda,\Omega',\Omega) = [VC \times (\rho_{unscat}(\lambda,\Omega',\Omega) + \rho_{singsc}(\lambda,\Omega',\Omega) + \rho_{multsc}(\lambda,\Omega'))] + [(1-VC) \times \rho_{ground}(\lambda,\Omega',\Omega)] \tag{9}$$

The pixel reflectance arises from the area covered by vegetation within the pixel, indicated by the fractional vegetation cover, VC, and from exposed ground, indicated by the 1-VC term. As shown in the second line of (9), within the vegetation, there are three major components of the calculated reflectance ($\rho_{canopy}(\lambda,\Omega',\Omega)$): (1) radiation that is not scattered by vegetative tissues ($\rho_{unscat}(\lambda,\Omega',\Omega)$), (2) singly scattered radiation ($\rho_{singsc}(\lambda,\Omega',\Omega)$), and (3) radiation that undergoes multiple scattering ($\rho_{multsc}(\lambda,\Omega')$). Here, Ω' represents a unit vector in the direction of radiation propagating from the sun with zenith $\mu' = \cos\theta'$ and azimuth ϕ', and Ω represents a unit vector pointing from the pixel to the sensor with geometric position $\mu = \cos\theta$ and azimuth ϕ.

[28] Equation (9) can be rewritten as:0

$$\rho_{pixel}(\lambda,\Omega',\Omega) = \Bigg[VC \Bigg(\rho_{ground}(\lambda,\Omega',\Omega) \exp\Big[-\beta\Big(\frac{G(\Omega')}{|\mu'|} + \frac{G(\Omega)}{\mu}\Big) LAI\Big] + \frac{\Gamma(\lambda,\Omega',\Omega)}{|\mu'|\mu} \int_{LAI} \exp\Big[-\beta\Big(\frac{G(\Omega')}{|\mu'|} + \frac{G(\Omega)}{\mu}\Big) L\Big] dL + \rho_{multsc}(\lambda,\Omega') \Bigg) \Bigg] + \Big[(1-VC)\rho_{ground}(\lambda,\Omega',\Omega)\Big] \tag{10}$$

A full explanation of each component of (10) is given by *Myneni et al.* [1989], *Iaquinta and Pinty* [1994], *Asner and Wessman* [1997], and *Asner* [2000]. Briefly described here, the unscattered radiation is a function of the ground reflectance ($\rho_{ground}(\lambda, \Omega', \Omega)$), total canopy LAI, a canopy clumping parameter (β), the "G-function", and solar-viewing geometry. The G-function is given by Ross, [1981] as a function of the angular distribution of leaf normals. The radiation scattered once by canopy elements is a function of the solar-viewing geometry, β, G-function, LAI, and the gamma function, $\Gamma(\lambda,\Omega',\Omega)$. The gamma function is given by:

$$\Gamma(\lambda,\Omega',\Omega) = \frac{1}{2\pi}\int_{2\pi} f(\lambda,\Omega',\Omega;\Omega_L) g_L(\Omega_L) |\Omega_L \cdot \Omega'| d\Omega_L \tag{11}$$

where $g_L(\Omega_L)$ is the leaf normal distribution function as a function of the leaf normal unit vector Ω_L [*Ross* 1981], and $f(\lambda, \Omega', \Omega;\Omega_L)$ is the bi-lambertian function describing leaf

reflectance ($\rho_{\text{foliage}}(\lambda)$) and transmittance ($\tau_{\text{foliage}}(\lambda)$) [*Asner and Wessman*, 1997]:

$$f(\lambda,\Omega';\Omega;\Omega_L) = (\rho_{\text{foliage}}(\lambda)|\Omega_L\cdot\Omega|)/\pi; \quad (\Omega_L\cdot\Omega)(\Omega_L\cdot\Omega')<0$$
$$(\tau_{\text{foliage}}(\lambda)|\Omega_L\cdot\Omega|)/\pi; \quad (\Omega_L\cdot\Omega)(\Omega_L\cdot\Omega')<0 \tag{12}$$

The multiple scattering term in (10) is a function of leaf reflectance and transmittance, the G-function, and solar geometry as specified by *Iaquinta and Pinty* [1994]; it is independent of viewing geometry.

[29] Based on equations (9)–(12), the pixel-scale spectroscopic reflectance signature of a forest canopy is determined by a set of parameters representing foliage reflectance and transmittance, ground reflectance and canopy volume and architecture:

$$(\text{Hyperspectral Reflectance}_\lambda) = M_{hyper}\begin{pmatrix} LAI \\ \rho_{foliage}(\lambda),\tau_{foliage}(\lambda) \\ \rho_{ground}(\lambda,\Omega'\Omega) \\ G-Function \\ \beta \\ VC \end{pmatrix} \tag{13}$$

Variation in the magnitude and shape of the hyperspectral reflectance continuum from 0.4–2.5 μm is dependent upon the spatial variation of the parameters above [*Jacquemoud*, 1993; *Asner*, 1998]. However, in nature, the range of variability may be large for some parameters while it is narrow for others. For example, tissue optical properties ($\rho_{\text{foliage}}(\lambda)$, $\tau_{\text{foliage}}(\lambda)$), ground reflectance ($\rho_{\text{ground}}(\lambda)$), and leaf angle distribution (G-function) vary within a relatively narrow range of values in most ecosystems [*Asner et al.*, 1998c], especially in conifer forests [e.g., *Mesarch et al.*, 1999]. In many coniferous forests, the parameters that vary at the highest spatial frequency tend to be LAI and VC [*Cohen et al.*, 1996]. Thus, solving (13) can be achieved by allowing the parameters that are not of interest to be constrained to ranges of variability as prescribed from large field-based data bases, while parameters of interest (LAI, VC) are estimated.

[30] It should be noted that the hyperspectral reflectance actually depends on LAD(z), and therefore on Rel(z;$\vec{P}$), which formally should be included in the parameter vector in (13). The dependence on the relative density has been effectively ignored in (10) by taking Rel(z;$\vec{P}$) to be independent of z, which leads to the separate parameter estimations in (3). Because the radar dependence on Rel(z;$\vec{P}$) is much stronger than the hyperspectral dependence, this probably introduces errors that are negligible compared to the dominant errors mentioned in section VII on results.

[31] The solution to (13) is carried out in two steps. First, spectral derivatives in the shortwave-infrared (SWIR, 2.0–2.4 μm) region are used to estimate VC. Spectral derivatives in this region have been shown to provide the most robust information on the (horizontal or lateral) extent of dominant land-cover such as green canopy and soil/dry needles as apparent to the sensor [*Asner and Lobell*, 2000]. When the effect of spectral albedo is removed via the use of derivative spectra, (10) converges on a linear solution involving derivative spectra, $\left|VC\frac{d\rho_{canopy}(\lambda,\Omega'\Omega)}{d\lambda}\right| + \left|(1-VC)\frac{d\rho_{ground}(\lambda,\Omega'\Omega)}{d\lambda}\right|$, where ρ_{canopy} is as in (10). We have already demonstrated that the derivative-SWIR spectral unmixing provides canopy cover information independent of variation in LAI in these conifer forests [*Lobell et al.*, 2001].

Table 1. Basic Characteristics of Each Coniferous Forest Stand for Which LAD Was Estimated

Plot Number	Longitude	Latitude	Description
1	−121°37′29.2″	44°29′55.6″	multilayer, tall old-growth and short, young trees
2	−121°37′21.8″	44°30′1.8″	open and uniform, single layer tall canopy
3	−121°37′21.9″	44°29′54.2″	dense stand, with a single layer of short trees, and a few large old trees

[32] The second step requires a numerical inversion of a photon transport model (equations 9–12) to estimate LAI [*Asner et al.*, 1998b]. The model inversion is executed within a Monte Carlo scheme that allows $\rho_{\text{foliage}}(\lambda)$, $\tau_{\text{foliage}}(\lambda)$, ($\rho_{\text{ground}}(\lambda)$), the G-function, and β to be varied along with LAI. The VC parameter is fixed to the value derived from the first stage SWIR analysis. The estimated LAI value is that which provides the best fit between measured and modeled AVIRIS spectra [*Asner et al.*, 1998a, 1998c; *Asner*, 2000]. The final LAI estimates include standard error ranges, which arise from the use of Monte Carlo methods for the narrowly defined free-floating parameters. The LAI estimate is achieved using only the visible and near-IR wavelengths from 0.55–1.25 μm; this region is extremely sensitive to variation in LAI [*Hall et al.*, 1990; *Gao and Goetz*, 1995; *Ustin et al.*, 1998].

6. Leaf Area Density From Field Measurements

[33] This section describes leaf area density estimations from field measurements of three stands located at the Metolius flux site in Central Oregon. Three stands were selected with different canopy structures and stand densities. LADs from these stands will be compared to remotely sensed parameter estimates in the next section. The stands are described in Table 1. Due to high stand density in the short canopy plot (plot 3) trees were measured on five 10 m radius subplots as opposed to measuring all of the trees on the plot. In mixed canopy plots (1 and 3), we identified two size classes: trees less than 30 cm DBH and trees greater than 30 cm DBH. These three stands have structures similar to those in logged and undisturbed forests [*Law et al.*, 2001a, 2001b].

[34] In CANLAD, a model developed to produce LAD at the stand level, the field-measured LAI was apportioned as a function of height above the ground by calculating the fractional canopy volume containing most of the leaf area, as a function of height. Calculations of canopy volume were made using two functions, one for the volume from the base of the crown to the widest point of the crown and one for the volume from the widest point of the crown to the top of the crown, represented in the two terms of (14). The crown radius at any altitude z in the tree was assumed to vary as the fourth root of the fractional distance to the bottom or top of the tree, for each volume respectively. Field work

Table 2. The LAD Parameters Estimated From the Radar and Hyperspectral Data for Three Coniferous Forest Plots, With Standard Errors in Parentheses

Plot Number	Radar		Hyperspectral
	Gaussian Center z_G, m	Gaussian Standard Deviation, σ_G, m	Leaf Area Index (LAI), m^2/m^2
1	0.0 (1.1)	16.7 (1.2)	1.8 (0.4)
2	25.2 (1.6)	5.3 (2.1)	1.1 (0.3)
3	12.8 (7.2)	13.2 (3.4)	2.4 (0.4)

suggested that the fourth root best approximates the profile of a typical ponderosa pine. The sum of these two volumes yields the volume of the entire tree canopy as a function of field-measured quantities:

$$V(x, z_b, z_w, z_t) = \pi \int_{z_b}^{z_w} x^2 \sqrt{\frac{z - z_b}{z_w - z_b}} dz + \pi \int_{z_w}^{z_t} x^2 \sqrt{\frac{z_t - z}{z_t - z_w}} dz \quad (14)$$

where V = canopy volume, z_t = tree height, z_w = height at widest point of crown, z_b = height at base of crown, z = integration variable, and x = crown radius at widest point of crown.

[35] Because leaf area is concentrated distal to the main stem, an outer shell of leaf area was produced by using the same formula, but reducing canopy dimensions by 1–2 m [*Cescatti*, 1997a]. Thus, the volume between the stem and the terminal branches was subtracted, leaving an outer shell that typically contains most of the leaf area. Field measurements were taken in order to determine how 'deep' this outer shell should be.

[36] This tree canopy shell was then divided into 1m layers horizontally (e.g., 0–1 m, 1–2 m, etc.), and a volume was calculated for each bin and averaged to obtain mean stand volume for each bin. Stand LAI was then distributed in the bins according to the percentage of canopy volume within each bin. For stand 1 (mixed canopy structure), we used a mean bin volume weighted by total stand canopy volume for each of the two size classes. The final product of the model is an LAD value for each 1m bin, where each bin represents a mean value for the entire plot.

7. LAD Results of the Central-Oregon Demonstration

[37] Remote sensing determinations of LAD are the central result of this paper. Combining Gaussian center, z_G, and the standard deviation, σ_G, estimated from the AIRSAR radar data, with the LAI estimated from the AVIRIS hyperspectral data yields LAD(z). Table 2 shows the radar and hyperspectral parameter estimates and their standard errors in parentheses. The standard errors are calculated by putting a distribution about the actual data into the mechanism of Figure 2, in place of the data box. Simulated observations and ranges of constrained parameters (in the hyperspectral estimation) are fed to the process in Figure 2 in a Monte Carlo analysis. The statistics of the optimal parameters estimated from the Monte Carlo trials determine the parameter estimate standard errors.

[38] Field estimates of LAD were derived as described in the previous section. They were based on the field measurements shown below in Table 3 along with the field-measured LAI values. The number of trees per hectare is also shown for reference.

[39] Figures 5a, 5b and 5c, show field-measured LAD for plots 1, 2, and 3, along with LAD estimated from the radar and hyperspectral data, from the parameters in Table 2. Also shown are error bars on two points of the field-measurement curve. These standard errors were derived by comparing stand 1 results to results from a three-dimensional radiative transfer model driven by the field measurements [*Law et al.*, 2001a, *Cescatti*, 1997a; *Cescatti*, 1997b]. The error bar is higher at lower altitudes because the CANLAD model does not appear to adequately produce a crown-shape and leaf area distribution for shorter trees, partly because of the rather simple representation of the crown envelope. The 'R+H 1-sigma' dotted-line curve is formed by using both radar and hyperspectral parameters that are shifted by one standard error away from the best estimate, which is indicated by the solid 'Radar+ Hyperspectral' curve.

[40] The agreement between the field and remote sensing LAD determinations is often within 1–2 standard errors of the difference standard error (the quadrature sum of the individual standard errors). That is, either the solid remote sensing curves or the 1-sigma curves are within 1–2 standard deviations of the field measurements for much of the range of height above ground. The agreement between the remote sensing and field LAD is reasonable for stands 1 and 2. The largest disagreement is the failure of the radar plus hyperspectral curve to track the large peak for low heights in stand 3, Figure 5c. Part of the reason for this disagreement in stand 3 is that the Gaussian model used in the radar analysis, motivated by the need to keep the number of

Table 3. Field Measurements Used in Field LAD Estimation, With Standard Errors in Parentheses[a]

	Dbh, cm	x, m	z_b, m	Z_w, m	Z_t, m	Number Trees and aboveground Biomass (Tons) per Hectare
Plot 1;	13.13 (0.23)	1.40 (0.02)	4.46 (0.08)	5.94 (0.10)	9.52 (0.16)	753
LAI = 1.91 (0.03)	68.47 (3.25)	4.41 (0.22)	9.51 (0.47)	19.20 (0.98)	33.85 (1.32)	178
Plot 2;	54.95 (2.51)	2.97 (0.06)	12.09 (0.48)	19.24 (0.61)	33.48 (1.26)	84
LAI = 0.89 (0.01)						227
Plot 3;	12.47 (0.40)	1.34 (0.01)	6.27 (0.15)	6.91 (0.16)	10.63 (0.30)	1286
LAI = 2.45 (0.04)	55.24 (4.25)	2.19 (0.50)	12.42 (0.97)	17.95 (0.85)	30.95 (1.56)	277

[a] For the geometric measurements in mixed-canopy plots, the top entry is for shorter trees (<15 m) and the lower entry is for taller trees.

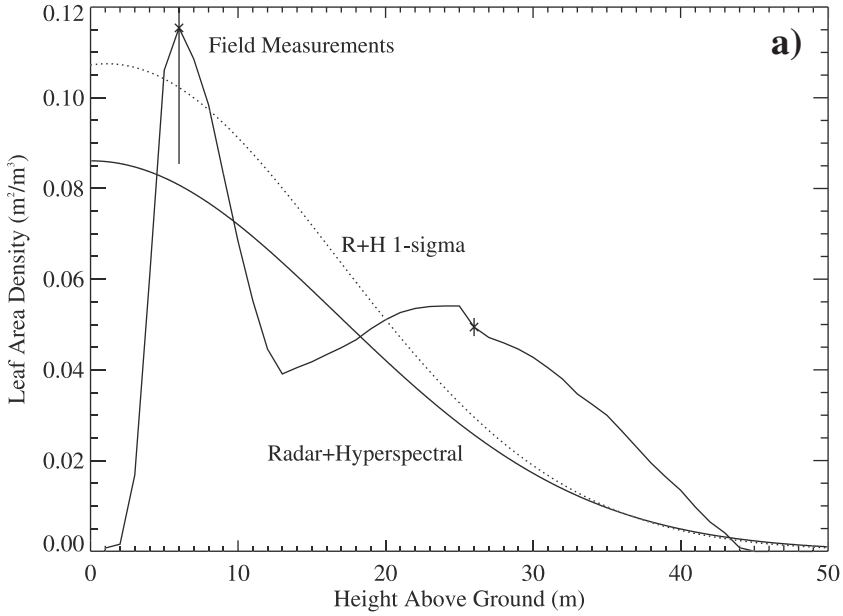

Figure 5a. Plot 1 LAD from field measurements and radar + hyperspectral quantitative fusion LAD estimate. The dotted line is the LAD generated with parameters 1-sigma away from the best estimates.

estimated parameters small, is not the best description of the LAD for stands 1 or 3. Because forcing the remote-sensing profile to look Gaussian is akin to measuring the best Gaussian which fits the field data, that best-fit Gaussian is shown with the remote sensing profiles in Figure 6. The performance of the remote sensing data at the large peak is improved, with slightly worse agreement at higher heights. Figure 6 suggests that the remote sensing parameter estimation process might be able to find the best Gaussian fit to LAD, but that even the best Gaussian does not fit the field LAD that well.

[41] Figures 5 and 6 suggest that if the radar profile model could be made more complex, for example a double Gaussian or Gaussian with a pedestal, the remote-sensing LAD determination could be more accurate. More diverse observations would be required than were available in this data set, if more complex models with more parameters were used. As already noted for this radar data set, redundancy was built in. Estimating phase-offset parameters due to systematic AIRSAR interferometric effects, as indicated in (8), also limited the number of new structure parameters that could be introduced into this analysis. In the future, altitudes that are not multiples of each other will be flown, and phase calibration will be done at different AIRSAR altitudes. There may be other radar model inadequacies, for example flaws in the assumptions in (5), which can be

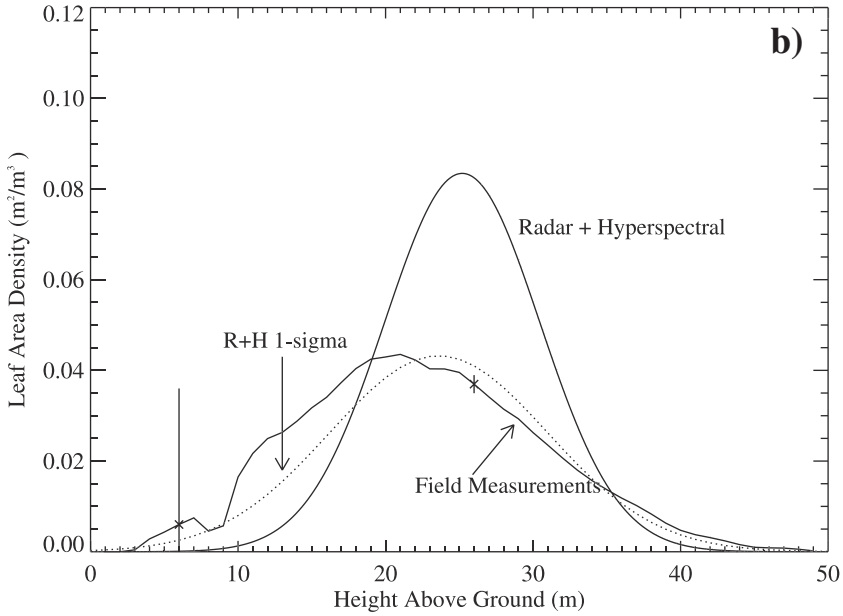

Figure 5b. Plot 2 LAD from field measurements and radar + hyperspectral quantitative fusion.

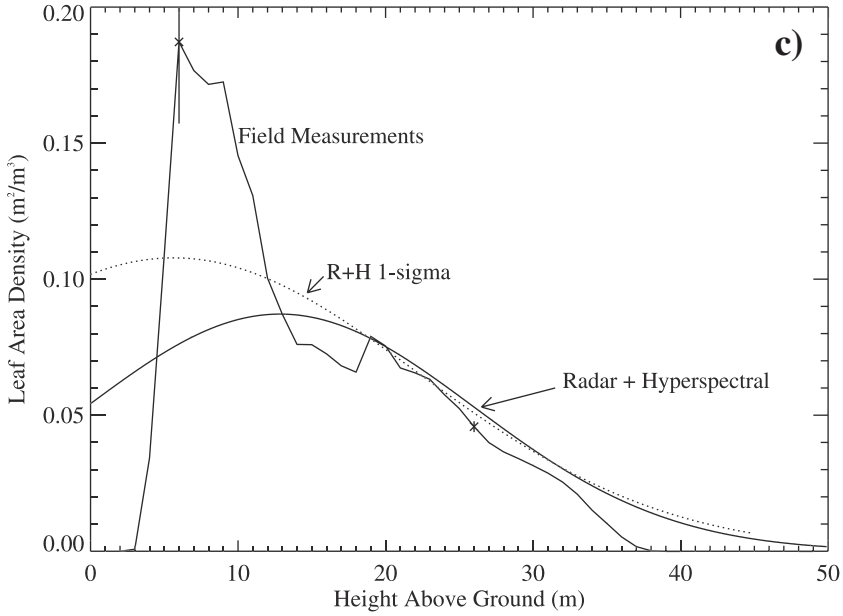

Figure 5c. Plot 3 LAD from field measurements and radar + hyperspectral quantitative fusion LAD estimate.

explored with more diverse data sets. The LAD from remote sensing and the field estimates should ultimately agree within one standard error on average for all heights.

[42] The LAI values derived from the AVIRIS observations of the three plots were well within the error range that can be reported from field measurements [*Law et al.*, 2001b]. As shown in a few previous studies [e.g., *Asner et al.*, 1998b; *Ustin et al.*, 1998], spectroscopic radiance (reflectance) measurements provide a means to estimate LAI with relatively high accuracy, especially when LAI ranges from zero to five. However, the various methods for retrieving LAI are prone to errors resulting primarily from the partial cover of the canopy within image pixels. The greatest uncertainty in this approach is in several assumptions about the clustering of needles within the canopies (and the physical model) [*Myneni et al.*, 1989; *Chen*, 1996]. We have found that the LAI values retrieved from the inverse modeling method are highly sensitive to assumptions about needle clumping, as has been found in previous studies [*Law et al.*, 2001a, 2001b]. Our reported LAI estimates for the three study plots have uncertainty ranges of 0.3–0.4 LAI units due primarily to the uncertainty in needle clumping (data not shown).

[43] The CANLAD model used to estimate LAD from field data could be improved to include a more refined crown envelope with shape coefficients and three-dimen-

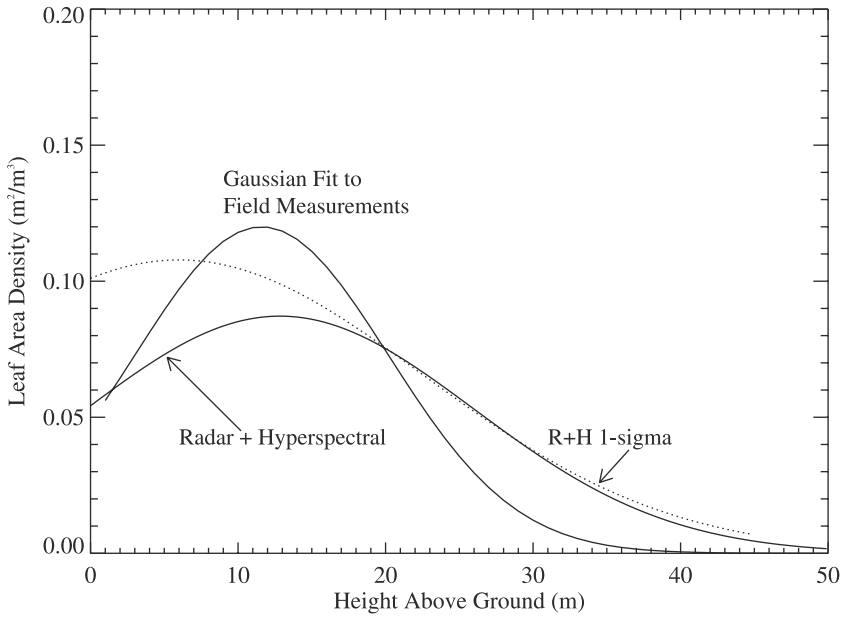

Figure 6. The best Gaussian fit to field estimates of LAD for plot 3, and radar + hyperspectral quantitative fusion estimate.

sional modeling (e.g. ellipse quadrants), accounting for asymmetry in crown geometry, as well as adding one or two more shells for distribution of leaf area within the crown envelopes. These features are in the FOREST model by *Cescatti* [1997a, 1997b]. LAD from the FOREST model is demonstrated in *Law et al.* [2001a], where the same field measurement approach was used for canopy dimension model parameters, and the model produced reasonable LADs.

[44] Some error in the relative density profiles may result from the difference in acquisition epochs of the radar (April 1998) and the field measurements (June 1999). The hyperspectral data were acquired coincident with the field data. The discrepancy between the remote sensing and field measurements at greater than 2 standard errors in Figure 5 could also be due to model assumptions such as those in (5). Other assumptions in the radar and hyperspectral models should be investigated, as well as the model assumptions in estimating LAD from field data.

8. Conclusions and Plans

[45] This paper describes and demonstrates a quantitative approach to the fusion of radar and hyperspectral data for the estimation of the leaf area density of forests, which bears on carbon sequestration and change due to biomass dynamics. Multialtitude AIRSAR radar interferometric and polarimetric data as well as AVIRIS hyperspectral-optical data were acquired over the Metolius flux site in Central Oregon. Quantitative, model-driven parameter estimation applied to the combined data set yielded LAD(z). This approach potentially applies to the estimation of many parameters of interest describing vegetated land surfaces from remotely sensed data.

[46] In this first attempt at LAD determination from remote sensing data, the radar interferometric and polarimetric data were analyzed with a physical model and estimation procedure separately from the hyperspectral data. A relative density profile was estimated from the radar data, and a normalizing LAI was estimated from the hyperspectral data to determine the LAD. The multialtitude interferometric data were most responsible for the relative density profile, with some enhancement from the polarimetric horizontal to vertical power ratio. The hyperspectral data provided estimates of sub-pixel canopy cover [*Lobell et al.*, 2001] and LAI. Field estimates of LAD were obtained from geometric measurements of trees and LAI data and a physical model. The remote sensing agreement with the field LAD was usually within 1–2 standard errors, suggesting that some systematic errors were underestimated.

[47] One systematic error in the modeling effort probably results from assuming Gaussian LAD profiles, when some of the actual profiles are not Gaussian. The AVIRIS-derived LAI measurements could be improved by incorporating a better representation of conifer needle geometry and clumping, both of which are known to cause errors in the estimate of LAI in these forest types [*Chen*, 1996]. In addition, the CANLAD model used on the field data likely had systematic errors when short trees were encountered, because of the simplified representation of the crown envelope.

[48] Future attempts at combining interferometric and polarimetric radar with hyperspectral data will include flying altitudes that are not multiples of each other. This will diversify the data set and allow the estimation of additional profile parameters to address the departure from Gaussian behavior of the actual LAD profiles. Systematic phase errors in the AIRSAR data, which forced the introduction of phase offset parameters at the cost of the LAD accuracy, will be phase calibrated more accurately in future studies (E. O'Leary, personal communication, 2001). Future analysis of the accuracy of the LAI estimation will be made using all 20 forest plots and an improved photon transport model with a better representation of needle clumping [*Law et al.*, 2001a; *Chen and Black*, 1992; *Gower and Norman*, 1991]. The CANLAD model will be improved with crown shape coefficients to better represent crown structure of short canopies.

[49] In future approaches to data fusion, all observations from all data types will be analyzed in a unified model, as in Figure 2, as opposed to the separate radar and hyperspectral approaches in this work. For example, future quantitative-fusion estimations of LAD(z) will include the explicit dependence of both radar and hyperspectral on $\mathrm{Rel}(z;\vec{P})$, which was suppressed in (10) and (13). Other observation dependences on common parameters that have been ignored in this first demonstration of quantitative fusion will be incorporated in future unified parameter estimations. Scenarios in which common parameters are simultaneously estimated from multiple sensors should improve accuracy and facilitate the detection of systematic errors, particularly when the observation vector is sufficiently diverse to allow more complex, realistic relative density profiles. Including lidar data [*Lefsky et al.*, 1999], for example, and a lidar physical model along with radar and hyperspectral analyses will further improve performance. A unified approach to quantitative data fusion will yield the estimation of LAD(z) and other common structural parameters; this will greatly facilitate global monitoring of biomass and carbon dynamics.

[50] **Acknowledgments.** We thank D. Lobell and K. Cody for their assistance with field and modeling analyses. We also thank E. O'Leary, T. Miller, A. Chu, C. Jennison, and the JPL AIRSAR group for acquiring and processing the radar data. J. Faust and R. Green and the AVIRIS group are gratefully acknowledged for acquiring and processing the hyperspectral data. Johnner Barrett is acknowledged for contributions to the development of the CANLAD model and for mathematical consultations. This work was supported by NASA OES grant NAG5–8320 (RTOP 622–93–63–40). G. Asner was also supported by NASA New Millenium Program grant NAG5–5253. The research described in this paper was carried out in part at the Jet Propulsion Laboratory, California Institute of Technology, under a contract with the National Aeronautics and Space Administration.

References

Askne, J., P. Dammert, L. Ulander, and G. Smith, C-band repeat-pass interferometric SAR observations of forest, *IEEE Trans. Geosci. Remote Sens.*, *35*, 25–35, 1997.

Asner, G. P., Biophysical and biochemical sources of variability in canopy reflectance, *Remote Sens. Environ.*, *64*, 234–253, 1998.

Asner, G. P., A hyperspectral photon transport system for simulating imaging spectrometer observations of terrestrial ecosystems, paper presented at the 9th Annual JPL Airborne Earth Science Workshop, Pasadena, Calif., 2000.

Asner, G. P., and D. B. Lobell, A biogeophysical approach for automated SWIR unmixing of soils and vegetation, *Remote Sens. Environ.*, *74*, 99–112, 2000.

Asner, G. P., and C. A. Wessman, Scaling PAR absorption from the leaf to landscape level in spatially heterogeneous ecosystems, *Ecol. Modell.*, *103*, 81–97, 1997.

Asner, G. P., C. A. Bateson, J. L. Privette, N. Z. El Saleous, and C. A. Wessman, Vegetation structural effects on carbon uptake using satellite data fusion and inverse modeling, *J. Geophys. Res.*, *103*, 28,839–28,853, 1998a.

Asner, G. P., C. A. Wessman, and D. S. Schimel, Heterogeneity of savanna canopy structure and function from imaging spectrometry and inverse modeling, *Ecol. Appl.*, *8*, 926–941, 1998b.

Asner, G. P., C. A. Wessman, D. S. Schimel, and S. Archer, Variability in leaf and litter optical properties: implications for canopy BRDF model inversions using AVHRR, MODIS, and MISR, *Remote Sens. Environ.*, *63*, 200–215, 1998c.

Cescatti, A., Modelling the radiative transfer in discontinuous canopies of asymmetric crowns, I, Model structure and algorithms, *Ecol. Model*, *101*, 263–274, 1997a.

Cescatti, A., Modelling the radiative transfer in discontinuous canopies of asymmetric Crowns, II, Model testing and application in a Norway spruce stand, *Ecol. Model*, *101*, 275–284, 1997b.

Chen, J. M., Optically-based methods for measuring seasonal variation of leaf area index in boreal conifer stands, *Agric. For. Meteorol.*, *80*, 135–163, 1996.

Chen, J. M., and T. A. Black, Foliage area and architecture of plant canopies from sunfleck size distributions, *Agric. For. Meteorol.*, *60*, 249–266, 1992.

Chen, J. M., P. D. Blanken, T. A. Black, M. Guilbeault, and S. Chen, Radiation regime and canopy architecture in a boreal aspen forest, *Agric. For. Meteorol.*, *86*, 107–125, 1997.

Cloude, S. R., and K. P. Papathanassiou, Polarimetric SAR Interferometry, *IEEE Trans. Geosci. Remote Sens.*, *36*, 1551–1565, 1998.

Cohen, W. B., M. E. Harmon, D. O. Wallin, and M. Fiorella, Two decades of carbon flux from forests of the Pacific Northwest, *BioScience*, *46*, 836–844, 1996.

Diner, D. J., G. P. Asner, R. Davies, J.-P. Muller, B. Pinty, C. B. Schaaf, and J. Stroeve, New directions in Earth observing: Scientific applications of multiple-view-angle remote sensing, *Bull. Am. Meteorol. Soc.*, *80*, 2209–2228, 1999.

Gao, B. C., and A. F. H. Goetz, Column atmospheric water vapor and vegetation liquid water retrievals from airborne imaging spectrometer data, *J. Geophys. Res.*, *95*, 3549–3564, 1990.

Gao, B.-C., and A. F. H. Goetz, Retrieval of equivalent water thickness and information related to biochemical components of vegetation canopies from AVIRIS data, *Remote Sens. Environ.*, *52*, 155–162, 1995.

Gao, B.-C., K. B. Heidebrecht, and A. F. H. Goetz, Derivation of scaled surface reflectance from AVIRIS data, *Remote Sens. Environ.*, *44*, 165–178, 1993.

Gower, S. T., and J. M. Norman, Rapid estimation of leaf area Index In conifer and broadleaf plantations, *Ecology*, *72*, 1896–1900, 1991.

Green, R. O., M. L. Eastwood, and O. Williams, Imaging spectroscopy and the Airborne Visible/Infrared Imaging Spectrometer (AVIRIS), *Remote Sens. Environ.*, *65*, 227–240, 1998.

Hagberg, J. O., L. M. H. Ulander, and J. Askne, Repeat-pass SAR interferometry over forested terrain, *IEEE Trans. Geosci. Remote. Sens.*, *33*, 331–340, 1995.

Hall, F. G., K. F. Huemmrich, and S. N. Goward, Use of narrow-band spectra to estimate the fraction of absorbed photosynthetically active radiation, *Remote Sens. Environ.*, *32*, 47–54, 1990.

Iaquinta, I., and B. Pinty, Adaptation of a bidirectional reflectance model including the hot-spot to an optically thin canopy, in paper presented at the Sixth ISPRS International Symposium on Physical Measurements and Signatures in Remote Sensing, Val d'Isere, France, 1994.

Jacquemoud, S., Inversion of the PROSPECT+SAIL canopy reflectance model from AVIRIS equivalent spectra: Theoretical study, *Remote Sens. Environ.*, *44*, 281–292, 1993.

Kynazikhin, Y., J. V. Martonchik, R. B. Myneni, D. J. Diner, and S. W. Running, Synergistic algorithm for estimating vegetation canopy leaf area index and fraction of absorbed photosynthetically active radiation from MODIS and MISR data, *J. Geophys. Res.*, *103*, 32,257–32,275, 1998.

Landsberg, J. J., and R.H. Waring, A generalised model of forest productivity using simplified concepts of radiation-use efficiency, carbon balance and partitioning, *Forest Ecol. Manage.*, *95*, 209–228, 1997.

Law, B. E., R. H. Waring, P. M. Anthoni, and J. D. Aber, Measurements of gross and net ecosystem productivity and water vapor exchange of a *Pinus ponderosa* ecosystem, and an evaluation of two generalized models, *Global Change Biol.*, *6*, 155–168, 1999.

Law, B. E., M. Williams, P. Anthoni, D. D. Baldocchi, and M. H. Unsworth, Measuring and modeling seasonal variation of carbon dioxide and water vapor exchange of a *Pinus ponderosa* forest subject to soil water deficit, *Global Change Biol.*, *6*, 613–630, 2000.

Law, B. E., A. Cescatti, and D. D. Baldocchi, Leaf area distribution and radiative transfer in open-canopy forests: Implications to mass and energy exchange, *Tree Physiol.*, *21*, 777–787, 2001a.

Law, B. E., S. Van Tuyl, A. Cescatti, and D. D. Baldocchi, Estimation of leaf area index in open-canopy ponderosa pine forests at different successional stages and management regimes in Oregon, *Agric. Forest Meteorol.*, *108*, 1–14, 2001b.

Lefsky, M. A., W. B. Cohen, S. A. Acker, G. G. Parker, T. A. Spies, and D. Harding, Lidar remote sensing of the canopy structure and biophysical properties of Douglas-Fir western hemlock forests, *Remote Sens. Environ.*, *70*, 339–361, 1999.

Lobell, D. B., G. P. Asner, B. E. Law, and R. N. Treuhaft, Subpixel canopy cover estimation of coniferous forests in Oregon using SWIR imaging spectrometry, *J. Geophys. Res.*, *106*, 5151–5160, 2001.

Mesarch, M. A., E. A. Walter-Shea, G. P. Asner, E. M. Middleton, and S. S. Chan, A revised measurement methodology for conifer needle spectral optical properties, *Remote Sens. Environ.*, *68*, 177–192, 1999.

Myneni, R. B., J. Ross, and G. Asrar, A review on the theory of photon transport in leaf canopies, *Agric. Forest Meteorol.*, *45*, 1–153, 1989.

Rosen, P. A., S. Hensley, I. R. Joughin, F. K. Li, S. N. Madsen, E. Rodriguez, and R. M. Goldstein, Synthetic aperture radar interferometry, *Proc. IEEE*, *88*, 333–382, 2000.

Sellers, P. J., et al., Modeling the exchanges of energy, water, and carbon between continents and the atmosphere, *Science*, *275*, 502–509, 1997.

Treuhaft, R. N., and S. R. Cloude, The structure of oriented vegetation from polarimetric interferometry, *IEEE Trans. Geosci. Remote Sens.*, *37*, 2620–2624, 1999.

Treuhaft, R. N., and P. R. Siqueira, Vertical structure of vegetated land surfaces from interferometric and polarimetric radar, *Radio Sci.*, *35*, 141–177, 2000.

Treuhaft, R. N., S. N. Madsen, M. Moghaddam, and J. J. van Zyl, Vegetation characteristics and surface topography from interferometric radar, *Radio Sci.*, *31*, 1449–1485, 1996.

Tucker, C. J., and P. J. Sellers, Satellite remote sensing of primary production, *Int. J. Remote Sens.*, *7*, 1395–1416, 1986.

Ustin, S. L., D. A. Roberts, and A. Palacios-Orueta, Estimating canopy water content of chaparral shrubs using optical methods, *Remote Sens. Environ.*, *65*, 280–292, 1998.

Vermote, E. F., D. Tanre, J. L. Deuze, M. Herman, and J. J. Morcrette, Second simulation of the satellite signal in the solar spectrum, 6S: An overview, *IEEE Trans. Geosci. Remote Sens.*, *35*, 675–686, 1997.

Waring, R. H., and S. W. Running, *Forest Ecosystems, Analysis at Multiple Scales*, 2nd ed., 370 pp., Academic, San Diego, Calif., 1998.

Wegmuller, U., and C. Werner, Retrieval of vegetation parameters with SAR interferometry, *IEEE Trans. Geosci. Remote Sens.*, *35*, 18–24, 1997.

Whitehead, D., The estimation of foliage area from basal area in Scots pine, *Forestry*, *51*, 137–149, 1978.

Williams, M., B. E. Law, P. M. Anthoni, and M. H. Unsworth, Using a simulation model and ecosystem flux data to examine carbon-water interactions in ponderosa pine, *Tree Physiol.*, *21*, 287–298, 2001.

Zebker, H. A., S. N. Madsen, J. Martin, K. B. Wheeler, T. Miller, Y. Lou, G. Alberti, S. Vetrella, and A. Cucci, The TOPSAR interferometric radar topographic mapping instrument, *IEEE Trans. Geosci. Remote Sens.*, *30*, 933–940, 1992.

G. P. Asner, Department of Global Ecology, Carnegie Institution, Stanford, CA 94305, USA.

B. E. Law and S. Van Tuyl, College of Forestry, Oregon State University, Corvalis, Oregon 97331, USA.

Robert N. Treuhaft, Jet Propulsion Laboratory, 138–212, 4800 Oak Grove Drive, Pasadena, CA 91109, USA. (rnt@radar-sci.jpl.nasa.gov)